

AMPS: REAL-TIME MESH CUTTING WITH AUGMENTED MATRICES FOR SURGICAL SIMULATIONS*

YU-HONG YEUNG[†], ALEX POTHEN[†], AND JESSICA CROUCH[‡]

Abstract. We present the AMPS algorithm, a finite element solution method that combines principal submatrix updates and Schur complement techniques, well-suited for interactive simulations of deformation and cutting of finite element meshes. Our approach features real-time solutions to the updated stiffness matrix systems to account for interactive changes in mesh connectivity and boundary conditions. Updates are accomplished by an augmented matrix formulation of the stiffness equations to maintain its consistency with changes to the underlying model without refactorization at each timestep. As changes accumulate over multiple simulation timesteps, the augmented solution algorithm enables tens or hundreds of updates per second. Acceleration schemes that exploit sparsity, memoization and parallelization lead to the updates being computed in real-time. The complexity analysis and experimental results for this method demonstrate that it scales linearly with the problem size. Results for cutting and deformation of 3D elastic models are reported for meshes with node counts up to 50,000, and involve models of astigmatism surgery and the brain.

Key words. finite element, surgery simulation, real-time, deformable model, cutting

AMS subject classifications. 65F50, 65F10, 65F05, 65Y20

1. Introduction. We present an algorithm to support real-time deformation and cutting of solid finite element models by quickly solving the resulting time-varying equations. Topological mesh modifications and boundary condition changes are the basic operations of many simulation scenarios, particularly surgical simulations. Real-time finite element solution methods for mesh cutting is a computational challenge, first because graphic and haptic rendering demand accurate solutions at real-time update rates, and second because connectivity changes due to cutting and remeshing modifies the underlying matrix equations. Such modifications invalidate previous factorizations or inverse computations for the stiffness matrix, requiring either computationally expensive update procedures or solution via an iterative method.

Interactive simulations often involve unpredictable cutting paths to allow flexibility to the user inputs. This feature requires that the internal deformation of a solid model be computed and tracked so that accurate cut surfaces are exposed as cuts progress into a model’s potentially heterogeneous interior. While the 3D mesh is changed due to cutting, pushing and pulling forces are being applied, and new Dirichlet boundary conditions are being imposed by different fixation scenarios, a real-time solution method to compute the displacement of all nodes under these changes is essential to make the simulations practical.

Observing that the aforementioned changes to the meshes result in a principal submatrix update and a change in dimensions to the underlying equations, we propose a new solution approach to reflect both the update and the dimension change in a modified augmented matrix formulation. This approach is similar to other augmented matrix methods in that the matrix is represented in a block matrix form in which the (1,1) block is the fixed original matrix and the other blocks are either zero or vary

*This work was supported in part by NSF grant CCF-1637534; the U.S. Department of Energy through grant DE-FG02-13ER26135; and the Exascale Computing Project (17-SC-20-SC), a collaborative effort of the DOE Office of Science and the NNSA.

[†]Department of Computer Science, Purdue University, West Lafayette, IN (yyeung@purdue.edu, apothen@purdue.edu).

[‡]Department of Computer Science, Old Dominion University, Norfolk, VA (jrcrouch@cs.odu.edu).

according to the changes. The Schur complement operation is then applied to decouple the augmentation from the remaining part of the system, and the Schur complement system is solved in two phases. Our current solution combines a one-time sparse matrix-factorization for the (1,1) block with an explicit computation of a principal submatrix of the inverse of the original matrix and a direct solution of the Schur complement system. Sparsity in the matrix, solution vector, and the right-hand-side vector are carefully exploited throughout the computations and intermediate results are stored for subsequent changes in later cutting steps. The time complexity of the algorithm shows that performance scales well with model size and various cutting lengths, while supporting arbitrary cutting of any valid finite element mesh.

Different algorithms for mesh generation [2] [7] [10] [12], collision detection [14] [16] [19], and mesh refinement [5] [13] [15] can be paired with our solution algorithm to produce a complete simulation platform. Thus the scope of this paper does not include algorithms for simulation tasks other than solving the finite element system of equations. A feature of the solution algorithm presented is its flexibility to work with structured and unstructured meshes as well as a number of different methods for adapting mesh geometry to respect a cut surface.

The three main contributions of this work are:

- An augmented matrix formulation of the stiffness system of equations from a finite element model, specific for principal submatrix updates and dimension changes resulting from both continuous unpredictable cutting and imposition of new boundary conditions. This formulation keeps the original stiffness matrix as a submatrix to eliminate the necessity of re-factorization whenever a change occurs.
- A direct solution approach that provides fast and accurate solutions to both the updated portion and unchanged portion, when the percentage of mesh elements affected by topological changes is small.
- Acceleration of the solution method by exploiting sparsity, memoization and parallelization. We analyze the time complexity of the accelerated solution method using concepts from graph theory.

This paper is organized as follows. Section 2 reviews previous work on the real-time solution of physics-based models and finite element equations. Section 3 presents our new augmented method with principal submatrix update for assembling a finite element system of equations and accounting for changes in mesh connectivity and boundary conditions via updates to stiffness matrix factors. Section 4 presents speed and accuracy results from finite element deformation and cutting experiments with models of various size. Finally, Section 5 discusses conclusions and directions for future work.

2. Previous Work. The augmented matrix algorithm presented in this paper is related to those presented by us and our colleagues in [17] and [18]. In the first paper, we formed an augmented system to replace columns in the original matrix, and solved the Schur complement system using GMRES implicitly and the rest of the system directly using precomputed LDL^T factors of the original matrix. Symmetry of the system was destroyed during the update, and thus two closures needed to be computed to exploit the sparsities in both the matrix and the right-hand-side vector. The convergence of the iterative solver depended on the condition of the Schur complement of the system, and a preconditioner was sometimes needed for faster convergence. However, the absence of the explicit Schur complement made finding a fast and efficient preconditioner difficult.

To overcome these shortcomings, we follow an approach similar to that presented in the second paper. By observing that the only change to the original matrix is within a principal submatrix, with our co-authors we showed that symmetry could be preserved during the update. We presented two approaches to solve the Schur complement system, an iterative method and a direct method. However, the contingency analysis application for power grids considered there retained the size of the system for any contingency scenario. Thus the augmented system considered there applied to applications that do not change the matrix dimension. This is not the case with surgical simulations, in which new vertices are added to the mesh along the cutting surface. The additional vertices increase the overall dimension of the modified system. An extension is, therefore, presented in this paper to generalize the augmented matrix approach to systems where their dimensions change. We also improve the computation of the principal submatrix of the matrix inverse to further accelerate the solution.

In [18], CHOLMOD [3], an algorithm to update or downdate the Cholesky factor of the matrix with low-rank matrices, was compared to our augmented matrix formulation. It was shown that our approach outperformed CHOLMOD for the power contingency application. However, SuiteSparse, the software package that includes CHOLMOD, does not provide functionality to increase the dimension of the modified system. We, therefore, do not provide the comparison between our method and CHOLMOD for the surgical simulation application in this paper.

Other related papers were surveyed in the two aforementioned papers and hence we do not repeat them here.

3. Methods. In this paper we denote by n the order of the original matrix, m_t the number of its rows and columns replaced at time t , and k_t the change in dimension of the modified matrix at time t . Hence the modified matrix has order $(n + k_t)$. The original stiffness system is $Ka = f$, where the right-hand-side vector f is called the force vector. In the context of the finite element model used in the surgical simulation, m_t corresponds to the degrees of freedoms (DOFs) of the modified vertices and their neighbors, and k_t corresponds to the DOFs of the newly added vertices with respect to the original system. In general, $m_t \gg k_t$.

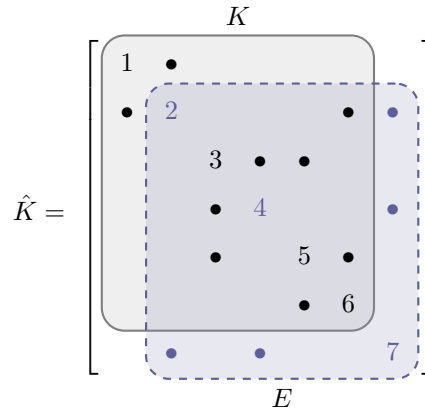


FIG. 1. Example of a modified (7×7) -matrix \hat{K} formed by a principal submatrix update E of size 3×3 enclosed in blue dashed box to the original (6×6) -matrix K enclosed in grey solid box with dimension change.

By considering the difference between the original $n \times n$ stiffness matrix K and the modified $(n + k_t) \times (n + k_t)$ stiffness matrix \hat{K} after cutting at time t as illustrated in Figure 1, we observe that \hat{K} can be expressed as the result of a principal submatrix update to K augmented by an identity matrix of size k_t :

$$(3.1) \quad \hat{K} = \underbrace{\begin{bmatrix} K & \\ & I_{k_t} \end{bmatrix}}_{\bar{K}} - \underbrace{\begin{bmatrix} H & \\ & I_{k_t} \end{bmatrix}}_{\bar{H}} \underbrace{\left(E + \begin{bmatrix} 0_{m_t} & \\ & I_{k_t} \end{bmatrix} \right)}_{\bar{E}} \underbrace{\begin{bmatrix} H^\top & \\ & I_{k_t} \end{bmatrix}}_{\bar{H}^\top},$$

where H comprises the m_t columns of the identity matrix of size n whose indices correspond to the rows and columns of K to be updated; and E is an $(m_t + k_t) \times (m_t + k_t)$ principal submatrix update to \bar{K} . Here H has dimension $n \times m_t$, \bar{H} has dimension $(n + k_t) \times (m_t + k_t)$; and \bar{E} has dimension $(m_t + k_t) \times (m_t + k_t)$, the same as that of E . Note that $\bar{H}^\top \bar{H} = I_{(m_t + k_t)}$.

If we express \hat{a} as the sum of two independent terms:

$$(3.2) \quad \hat{a} = \bar{a}_1 + \bar{H} \bar{a}_2$$

such that

$$(3.3) \quad \bar{H}^\top \bar{a}_1 = 0,$$

which implies $\bar{H}^\top \hat{a} = \bar{a}_2$, and let

$$(3.4) \quad \bar{a}_3 = \bar{H}^\top (\bar{f} - \hat{f}) - \bar{E} \bar{a}_2,$$

then with some arithmetic operations, we can show that a principal submatrix update in the form of Equation 3.1 can be solved using an augmented matrix formulation

$$(3.5) \quad \begin{bmatrix} \bar{K} & \bar{K} \bar{H} & \bar{H} \\ \bar{H}^\top \bar{K} & \bar{H}^\top \bar{K} \bar{H} - \bar{E} & 0 \\ \bar{H}^\top & 0 & 0 \end{bmatrix} \begin{bmatrix} \bar{a}_1 \\ \bar{a}_2 \\ \bar{a}_3 \end{bmatrix} = \begin{bmatrix} \bar{f} \\ \bar{H}^\top \hat{f} \\ 0 \end{bmatrix},$$

where \bar{f} is the $(n + k_t)$ -vector obtained by padding k_t zeros at the end of the force vector f , and \hat{f} is the force vector applied to the modified mesh. With \bar{K} as the pivot, Equation 3.5 can be reduced to a smaller system involving the symmetric matrix S_1 , the Schur complement of \bar{K} , and after multiplication with -1 we obtain:

$$(3.6) \quad \underbrace{\begin{bmatrix} \bar{E} & I \\ I & \bar{H}^\top \bar{K}^{-1} \bar{H} \end{bmatrix}}_{S_1} \begin{bmatrix} \bar{a}_2 \\ \bar{a}_3 \end{bmatrix} = \begin{bmatrix} \bar{H}^\top (\bar{f} - \hat{f}) \\ \bar{H}^\top \bar{K}^{-1} \hat{f} \end{bmatrix},$$

in which

$$(3.7) \quad \bar{K}^{-1} = \begin{bmatrix} K^{-1} & \\ & I_k \end{bmatrix}.$$

Equation 3.6 can be further reduced with another Schur complement using the $(1, 2)$ -block of S_1 as the block pivot:

$$(3.8) \quad \underbrace{(I - \bar{H}^\top \bar{K}^{-1} \bar{H} \bar{E})}_{S_2} \bar{a}_2 = \bar{H}^\top \bar{K}^{-1} \bar{f} - \bar{H}^\top \bar{K}^{-1} \bar{H} \bar{H}^\top (\bar{f} - \hat{f}) \\ = \bar{H}^\top \bar{K}^{-1} \hat{f}.$$

Note that the matrix S_2 is not symmetric. If \hat{f} only differs from f at the newly added vertices, i.e.

$$(3.9) \quad \hat{f} - \bar{f} = \begin{bmatrix} 0_n \\ \overset{\circ}{f} \end{bmatrix},$$

then the right-hand-side vector of Equation 3.8 can be simplified to

$$(3.10) \quad \bar{H}^\top \bar{K}^{-1} \hat{f} = \begin{bmatrix} H^\top a \\ \overset{\circ}{f} \end{bmatrix},$$

where a is the solution to the original system $Ka = f$ and $\overset{\circ}{f}$ is the force applied to the k_t newly added vertices.

After solving Equation 3.8 for \bar{a}_2 using a direct solver, we can solve for \hat{a} in the modified system $\hat{K}\hat{a} = \hat{f}$ directly using the following observation. Premultiplying the first row block of Equation 3.5 by \bar{K}^{-1} and rearranging the terms yields

$$(3.11) \quad \bar{a}_1 = \bar{K}^{-1} \bar{f} - \bar{H} \bar{a}_2 - \bar{K}^{-1} \bar{H} \bar{a}_3.$$

In addition, rearranging the terms in first row block of Equation 3.6 yields

$$(3.12) \quad \bar{a}_3 = \bar{H}^\top (\bar{f} - \hat{f}) - \bar{E} \bar{a}_2.$$

Substituting Equation 3.12 into Equation 3.11 yields

$$(3.13) \quad \bar{a}_1 = \bar{K}^{-1} \left[\bar{f} - \bar{H} \bar{H}^\top (\bar{f} - \hat{f}) \right] + (\bar{K}^{-1} \bar{H} \bar{E} - \bar{H}) \bar{a}_2.$$

Again, if \hat{f} satisfies the condition of Equation 3.9, Equation 3.13 can be simplified to

$$(3.14) \quad \bar{a}_1 = \begin{bmatrix} a \\ \overset{\circ}{f} \end{bmatrix} + (\bar{K}^{-1} \bar{H} \bar{E} - \bar{H}) \bar{a}_2.$$

Substituting Equation 3.14 into Equation 3.2 yields

$$(3.15) \quad \hat{a} = \begin{bmatrix} a \\ \overset{\circ}{f} \end{bmatrix} + \bar{K}^{-1} \bar{H} \bar{E} \bar{a}_2,$$

thus completing the solution.

An alternative Schur complement formulation is possible. One can use the $(2, 1)$ -block in Equation 3.6 as the block pivot for the Schur complement and get

$$(3.16) \quad \begin{aligned} (\bar{E} \bar{H}^\top \bar{K}^{-1} \bar{H} - I) \bar{a}_3 &= \bar{H}^\top (\hat{f} - \bar{f}) + \bar{E} \bar{H}^\top \bar{K}^{-1} \bar{f} \\ &= \begin{bmatrix} 0 \\ \overset{\circ}{f} \end{bmatrix} + \begin{bmatrix} E_{11} \\ E_{12}^\top \end{bmatrix} H^\top a, \end{aligned}$$

assuming that the condition in Equation 3.9 is satisfied. Again the coefficient matrix is not symmetric. After solving for \bar{a}_3 using Equation 3.16, the solution \hat{a} can be obtained as follows:

$$(3.17) \quad \hat{a} = \begin{bmatrix} a \\ \overset{\circ}{f} \end{bmatrix} - \bar{K}^{-1} \bar{H} \bar{a}_3.$$

3.1. Improving numerical accuracy. We can improve the numerical accuracy of the solutions by substituting \bar{a}_2 into \hat{a} directly as follows. From the third row block of Equation 3.5, we have

$$(3.18) \quad \bar{H}^\top \bar{a}_1 = 0.$$

Premultiplying Equation 3.2 by \bar{H}^\top yields

$$(3.19) \quad \bar{H}^\top \hat{a} = \bar{H}^\top \bar{a}_1 + \bar{H}^\top \bar{H} \bar{a}_2 = \bar{a}_2.$$

Note that the components of \hat{a} picked out by \bar{H}^\top correspond to \bar{a}_2 , which are arithmetically identical to the same components computed using Equation 3.15 but with higher accuracy. If we denote \mathbb{H} as the set of indices for which the rows and columns of A are updated including the newly added ones, combining the two equations, we have

$$(3.20) \quad \hat{a}[i] = \begin{cases} (\bar{H} \bar{a}_2)[i] & \text{for } i \in \mathbb{H}, \\ \left(\begin{bmatrix} a \\ f \end{bmatrix} + \bar{K}^{-1} \bar{H} \bar{E} \bar{a}_2 \right)[i] & \text{for } i \notin \mathbb{H}. \end{cases}$$

Skipping the computations of those components in \hat{a} that are in \mathbb{H} also improves the performance of the algorithm.

3.2. Computing the Schur Complement Matrix. Our augmented algorithm involves solving Equations 3.8 and 3.20. Unlike [17] both equations are solved using a direct solver. The Schur complement matrix S_2 in Equation 3.8 can be expressed in block matrix form using Equations 3.1, 3.7 and 3.10 to obtain

$$(3.21) \quad \left(\begin{bmatrix} I_m & \\ & 0_k \end{bmatrix} - \begin{bmatrix} H^\top K^{-1} H & \\ & I_k \end{bmatrix} E \right) \bar{a}_2 = \begin{bmatrix} H^\top a \\ f \end{bmatrix}.$$

Solving Equation 3.21 involves computing the principal submatrix of the inverse $H^\top K^{-1} H$. Assuming that $K = LDL^\top$ is a factorization of K , we have

$$(3.22) \quad H^\top K^{-1} H = H^\top L^{-\top} D^{-1} L^{-1} H.$$

If we denote $V \equiv L^{-1} H$, then $H^\top K^{-1} H = V^\top D^{-1} V$, which can be computed by first solving for V using forward substitution, then scaling V to obtain $U \equiv D^{-1} V$ and finally premultiplying U by V^\top . The computation of the rest of the matrix in Equation 3.21 is straight forward.

3.3. Memoization. For an efficient computation of the principal submatrix of the inverse $H_t^\top K^{-1} H_t$ at time t , we observe that since the vertices removed during the cutting are accumulating and H is the submatrix of the identity corresponding to the replaced rows and columns in K , the matrix H_{t-1} at the previous time $t-1$ is a submatrix of the first m_{t-1} columns of matrix H_t at time t , i.e.,

$$(3.23) \quad H_t = \begin{bmatrix} H_{t-1} & H_{\Delta t} \end{bmatrix},$$

where $H_{\Delta t}$ is the $(m_t - m_{t-1})$ columns of the identity matrix corresponding to the newly removed columns at timestep t . Consequently, the matrix V_{t-1} is also the first m_{t-1} columns of V_t since each column of V_t is independently solved, i.e.,

$$(3.24) \quad V_t = \begin{bmatrix} V_{t-1} & V_{\Delta t} \end{bmatrix},$$

where $V_{\Delta t} = L^{-1}H_{\Delta t}$, which are the only columns of V_t that need to be computed. Furthermore, the top-left $(m_{t-1} \times m_{t-1})$ submatrix of $H_t^\top K^{-1}H_t$ is identical to $H_{t-1}^\top K^{-1}H_{t-1}$ because

$$\begin{aligned}
 (3.25) \quad H_t^\top K^{-1}H_t &= V_t^\top D^{-1}V_t = \left[\begin{array}{c} V_{t-1}^\top \\ V_{\Delta t}^\top \end{array} \right] D^{-1} \left[\begin{array}{c|c} V_{t-1} & V_t^\top \end{array} \right] \\
 &= \left[\begin{array}{c|c} V_{t-1}^\top D^{-1}V_{t-1} & V_{t-1}^\top D^{-1}V_{\Delta t} \\ \hline V_{\Delta t}^\top D^{-1}V_{t-1} & V_{\Delta t}^\top D^{-1}V_{\Delta t} \end{array} \right] \\
 &= \left[\begin{array}{c|c} H_{t-1}^\top K^{-1}H_{t-1} & V_{t-1}^\top D^{-1}V_{\Delta t} \\ \hline V_{\Delta t}^\top D^{-1}V_{t-1} & V_{\Delta t}^\top D^{-1}V_{\Delta t} \end{array} \right].
 \end{aligned}$$

Furthermore, it can be observed from Equation 3.25 that $H_t^\top K^{-1}H_t$ is also symmetric and only the lower or upper triangular part needs to be computed and stored, and subsequent updates can be done sequentially by trapezoidal augmentations to $\text{tril}(H_{t-1}^\top K^{-1}H_{t-1})$:

$$(3.26) \quad \text{tril}(H_t^\top K^{-1}H_t) = \left. \begin{array}{c} \text{tril}(H_{t-1}^\top K^{-1}H_{t-1}) \\ \hline \text{tril}(H_{\Delta t}^\top K^{-1}H_t) \end{array} \right\} \begin{array}{l} m_{t-1} \\ m_t - m_{t-1} \end{array},$$

where $\text{tril}(\bullet)$ is the lower triangular part of the matrix and the augmentation part, $\text{tril}(H_{\Delta t}^\top K^{-1}H_t)$, can be computed as

$$(3.27) \quad \text{tril}(H_{\Delta t}^\top K^{-1}H_t)[i, j] = (V_{\Delta t}[i, *])^\top D^{-1}(V_t[j, *]) \quad \text{for } i \in [m_{t-1} + 1, m_t]; j \in [1, i].$$

It is obvious that Equation 3.27 can be computed in parallel for all i 's and j 's since they are independent of each other.

3.4. Dimension Shrinking. In the case of the imposition of Dirichlet boundary conditions, the dimension of the system is shrunk instead of expanded, unlike the case of cutting. The authors in [17] have shown that an augmented matrix system similar to Equation 3.5 is equivalent to the modified system of equations:

$$(3.28) \quad \begin{bmatrix} K & H \\ H^\top & 0 \end{bmatrix} \begin{bmatrix} a_1 \\ a_2 \end{bmatrix} = \begin{bmatrix} \hat{f} \\ 0 \end{bmatrix},$$

where $a_2 = -H^\top f$ is the newly unknown force and \hat{f} is given by

$$(3.29) \quad \hat{f}[i] = \begin{cases} f[i] - \sum_{j \in \mathbb{H}} K[i, j]a[j] & j \notin \mathbb{H}, \\ -\sum_{j \in \mathbb{H}} K[i, j]a[j] & j \in \mathbb{H}. \end{cases}$$

Similar to Equation 3.5, we can reduce Equation 3.28 to a smaller system using K as the pivot:

$$(3.30) \quad H^\top K^{-1} H a_2 = H^\top K^{-1} \hat{f}.$$

Note that the matrix on the left-hand side is the principal submatrix of the inverse $K^{-1}(H)$, which can be efficiently computed as described in previous subsections. The right-hand side can be computed using $V \equiv L^{-1}H$ as

$$(3.31) \quad H^\top K^{-1} \hat{f} = V^\top \underbrace{D^{-1}L^{-1}\hat{f}}_g.$$

After computing a_2 , a_1 can be computed using the first row block of Equation 3.28 as

$$(3.32) \quad \begin{aligned} a_1 &= K^{-1} (\hat{f} - H^\top a_2) \\ &= L^{-\top} D^{-1} L^{-1} (\hat{f} - H^\top a_2) \\ &= L^{-\top} (g - D^{-1} V a_2), \end{aligned}$$

in which g is already computed in Equation 3.31 and can be reused.

3.5. Complexity Analysis. The time complexity of principal submatrix updates using the symmetric augmented formulation can be summarized in Table 1. Both per cut and total update times are provided. The one-time factorization costs assume meshes with good separators for both 2D and 3D-meshes, of size $O(n^{1/2})$ and $O(n^{2/3})$, respectively. In the table, variables with subscript t are the values at time t , those with subscript Δt are the newly added values at time t , whereas those without any subscript are their maxima over all t . Recall that n is the size of the original matrix K , m is the size of the principal submatrix update H , k is the dimension change. In addition, \mathbb{H} is the set of indices of the nonzero rows of H , $|L|$ is the number of nonzeros in L , c is the total number of cuts, and $v = \max_j |V_{*,j}|$ is the maximum number of nonzeros in any column of V , which is equivalent to the maximum closure size of any vertex in the graph of $G(L)$. For a detailed discussion on the concepts of closure and the relations between sparse matrix computations and its corresponding graph, we refer the readers to [17]. The authors also discussed the theorems that are used to prove the upper bounds of the complexity of the AMPS algorithms.

The overall time complexity of the algorithm is dominated by either Step 2 (computing $\text{tril}(H_{\Delta t}^\top K^{-1} H_t)$) or Step 6 (solving for \hat{a}). The update steps in the AMPS algorithm have an overall time complexity of

$$(3.33) \quad O(m^2 v + c \cdot |L|).$$

3.6. Parallelization. We can observe that Steps 1–4 in the update steps in Table 1 are easily parallelizable from the facts that in Step 1 each columns of $V_{\Delta t}$ are independently solved, both Steps 2 and 3 involve matrix-matrix multiplications, and in Step 4 the R.H.S. of Equation 3.10 is formed by mapping. The parallelization of Step 5 and 6 is non-trivial, which is out of the scope of this paper. The parallel time complexity of the update steps in the algorithm for p processors is

$$(3.34) \quad O\left(\frac{m^2 v}{p} + c \cdot |L|\right).$$

Computation		Complexity
Amortized initialization:		
1	Compute LDL^\top factorization of K	$O(n^2)$ for 3D meshes; $O(n^{3/2})$ for 2D meshes
2	Compute $a = K^{-1}f$	$O(L)$
Real-time update steps:		
	per step	total
1	Solve for $V_{\Delta t}$	$O(\sum_{h \in \mathbb{H}_{\Delta t}} \text{closure}_L(h))$
2	Compute $\text{tril}(H_{\Delta t}^\top K^{-1} H_t)$	$O((m_{t-1} + 1 + m_t)m_{\Delta t} \cdot v_t)$
3	Form S_2	$O(m_t^2(m_t + k_t) + m_t)$
4	Form R.H.S. of Equation 3.10	$O(m_t)$
5	Solve for \bar{a}_2 in Equation 3.8	$O((m_t + k_t)^3)$
6	Solve for \hat{a} in Equation 3.20	$O(m_t \cdot v_t + L)$

TABLE 1
Summary of time complexity

3.7. Relation to previous augmented formulation. The authors in [17] presented a hybrid asymmetric augmented algorithm to perform a surgical simulation using finite element models as we do. In their formulation, the system is augmented in an unsymmetric manner:

$$(3.35) \quad \begin{bmatrix} \bar{K} & J \\ \bar{H}^\top & 0 \end{bmatrix} \begin{bmatrix} \bar{a}_1 \\ \bar{a}_2 \end{bmatrix} = \begin{bmatrix} \hat{f} \\ 0 \end{bmatrix},$$

where J consists of the $(m + k)$ columns of \hat{K} to replace the corresponding columns of \bar{K} . Note that we use \bar{H}^\top here for matrices with more columns than rows instead. They then split Equation 3.35 into two parts to solve for \bar{a}_1 and \bar{a}_2 respectively:

$$(3.36a) \quad \bar{H}^\top \bar{K}^{-1} J \bar{a}_2 = \bar{H}^\top \bar{K}^{-1} \hat{f} \quad \text{and}$$

$$(3.36b) \quad \bar{a}_1 = \bar{K}^{-1} (\hat{f} - J \bar{a}_2),$$

in which the first equation is solved by using GMRES whereas the second one is solved using a direct solver.

Since J is a submatrix of \hat{K} , it can be expressed in terms of \hat{K} as

$$(3.37) \quad J = \hat{K} \bar{H}.$$

Substituting Equation 3.1 into Equation 3.37 yields

$$(3.38) \quad \begin{aligned} J &= (\bar{K} - \bar{H} \bar{E} \bar{H}^\top) \bar{H} \\ &= \bar{K} \bar{H} - \bar{H} \bar{E}. \end{aligned}$$

Substituting Equation 3.38 into Equations 3.36a and 3.36b yields

$$(3.39a) \quad (I - \bar{H}^\top \bar{K}^{-1} \bar{H} \bar{E}) \bar{a}_2 = \bar{H}^\top \bar{K}^{-1} \hat{f} \quad \text{and}$$

$$(3.39b) \quad \bar{a}_1 = \bar{K}^{-1} \hat{f} - \bar{H} \bar{a}_2 + \bar{K}^{-1} \bar{H} \bar{E} \bar{a}_2,$$

in which the first equation is identical to Equation 3.8. Substituting Equation 3.12 into Equation 3.39b yields

$$(3.40) \quad \bar{a}_1 = \bar{K}^{-1} \hat{f} - \bar{H} \bar{a}_2 + \bar{K}^{-1} \bar{H} \left[\bar{H}^\top (\bar{f} - \hat{f}) - \bar{a}_3 \right],$$

which is identical to Equation 3.11 if the condition in Equation 3.9 is satisfied. Hence, the two augmented formulations are mathematically equivalent.

4. Results. The augmented matrix method for principal submatrix updates was evaluated through finite element cutting experiments with five model types. This section provides relevant implementation details and presents experimental data. We compare the performances of the following three approaches:

- AMPS algorithm presented in Section 3;
- Unsymmetric augmented matrix methods presented in [17] using a GMRES iterative solver, without preconditioning, and with two kinds of preconditioners: sparse approximate inverse (SPAI) and the diagonal matrix D from the initial LDL^\top factorization of the initial stiffness matrix; and
- Jacobi preconditioned or nonpreconditioned conjugate gradient (CG) iterative solver applied on $\hat{A}\hat{x} = \hat{b}$.

For the latter two approaches, only the best performing versions are included in the figures.

4.1. Implementation. All experiments were conducted on a compute node with two 16-core Intel Xeon Processors E5-2698 v3 (“Haswell”) at 2.3 GHz, and each core equipped with 64 KB L1 cache (32 KB instruction cache, 32 KB data cache) and 256 KB L2 cache; as well as a 40-MB shared L3 cache per socket. In addition, there are 128 GB DDR4 2133 MHz memory. All data represent times averaged over 20 runs unless overall time exceeds 30 minutes, in which case we averaged over 10 runs.

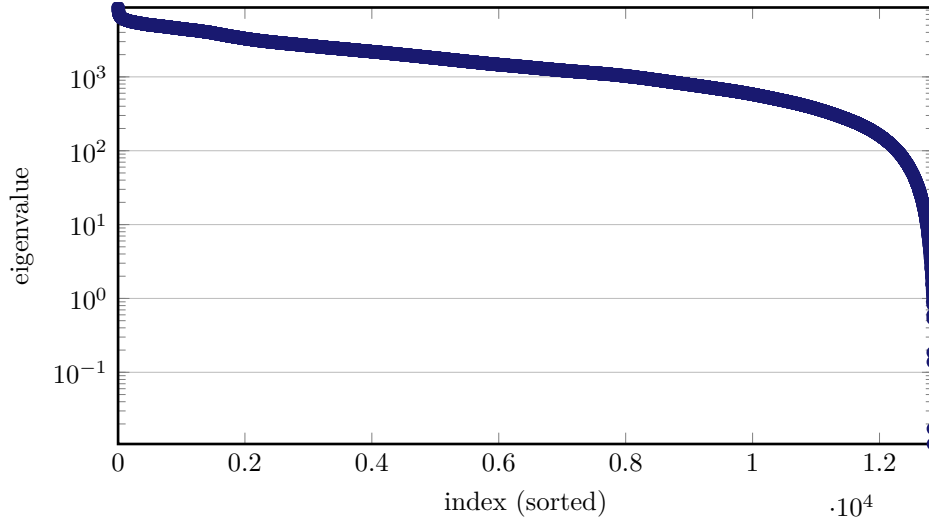
The precomputed LDL^\top factorizations of the stiffness matrices were computed using OBLIO, a sparse direct solver library [4]. All other basic linear algebra subroutines including matrix-vector products, dense matrix factorization and solves, as well as the GMRES iterative solver used in the unsymmetric augmented matrix methods and the CG solver used for comparison purposes were from the Intel Math Kernel Library (MKL) [8]. The remainder of the code, including the computation of the closure in K induced by $H_{\delta t}$, the matrices $V_{\Delta t}$ and $\text{tril}(H_{\Delta t} K^{-1} H_t)$ in Equation 3.27, and the overall algorithm, was written by the authors.

Since the closure of a set of indices in the graph of a triangular matrix can be found effectively column by column, and OBLIO uses supernodes in matrix factorization, the matrices K , L and V were stored in compressed sparse column matrix (CSC) format for efficient column access. The diagonal matrix D is stored in a vector of size n . The principal submatrix update E , the principal submatrix of the inverse $H^\top K^{-1} H$ and the Schur complement S_2 were stored in dense matrix format for fast computations. The matrix H and its transpose were represented as an array of indices and their multiplications with other matrices were done by index mappings. All vectors were stored in dense format.

4.2. Model Meshes. Four types of solid tetrahedral meshes were used for performance evaluation. The eye mesh rendering is shown in Figures 2 and the renderings of other meshes can be found in [17]. Table 2 lists for each mesh its number of vertices, the estimated condition number computed using Matlab’s `condest` function, and the factorization times computed using OBLIO. Since the models are 3-dimensional, the

FIG. 2. *Rendering of the eye mesh*

Mesh	$ V $	Estimated condition number	Factorization time (s)
Beam	100 – 25,600	$1.14 \times 10^3 - 3.29 \times 10^{12}$	0.02 – 1.62
Brick	250 – 18,081	$2.19 \times 10^3 - 1.18 \times 10^5$	0.1 – 5.42
Eye	17,821	7.73×10^6	1.6
Brain	50,737	failed to estimate	7.77

TABLE 2
Numerical properties of the meshes.FIG. 3. *Eigenspectrum of the eye mesh of 4,444 nodes.*

total degrees of freedom (DOFs) in each system are 3 times the number of vertices minus the DOFs constrained by the Dirichlet boundary conditions \mathcal{D} , which is also the dimension of the matrix, i.e., $n = 3|V| - |\mathcal{D}|$.

1. *Elongated Beam*: A group of five elongated rectangular solids with varying lengths were generated. Nodes were placed at regularly spaced grid points on a $5 \times 5 \times h$ grid, where h ranged from 4 to 1024. Each block mesh was anchored at one end of the solid. All elements had good aspect ratios and were arranged

in a regular pattern. However models with greater degrees of elongation produced more poorly conditioned systems of equations, as fixation at only one end meant that longer structures were less stable. Thus experiments with this group of meshes illuminates the way solver performance varies with stiffness matrix conditioning.

2. *Brick*: A group of five rectangular brick solids with varying mesh resolutions were generated. Each of the models had the same compact physical dimension of $1 \times 1 \times 2$. An initial good-quality mesh was uniformly subdivided to produce meshes of increasingly fine resolution. These meshes allowed us to examine solver performance relative to node count for fixed model geometry. Similar to the beam meshes, zero-displacement boundary conditions were applied to one face of the block.
3. *Eye*: A human eye model [1] with a clear corneal cataract incision was used in a simulation of corrective surgery for astigmatism. Zero displacement boundary conditions were applied to the posterior portion of the globe. Figure 3 shows the eigenspectrum of an eye mesh of 4,444 nodes, a downsampled mesh of the eye model.
4. *Brain*: A human brain model (contributed by INRIA to the AIM@SHAPE Shape Repository) was used to demonstrate applicability to surgical simulation on an organ of complicated structure. Zero displacement boundary conditions were applied to the interior portion of the brain. The condition number could not be estimated with Matlab due to insufficient memory.

On average, the nodes in the brick meshes have a higher degree of connectivity than those in the elongated beam meshes. This is due to a greater proportion of surface nodes present in the beam models versus interior nodes in the brick models. The increased connectivity leads to a higher percentage of nonzeros in the stiffness matrix factors and larger sizes for the closures referenced in Table 1. These differences have a significant impact on the relative performance of the solution methods.

4.3. Experiments. Performance was examined through two types of experiments: deformation of intact meshes through changes in boundary conditions, and deformation of meshes undergoing cutting.

4.3.1. Deformation of Intact Meshes. In this group of experiments, we applied an increasing number of non-zero essential boundary conditions to mesh nodes to create deformation. Figure 4 shows how solution time varied with the number of constrained nodes for instances of the beam and brick meshes.

For the beam mesh, AMPS outperformed the unsymmetric augmented matrix method by a factor of 1.65 and the CG method by 3.63, while maintaining a high average update rate of 343 Hz (updates/sec) throughout. The unsymmetric augmented matrix method came second, maintaining update rates around 200 Hz. CG performed the worst, providing updates in the range of 1.6–33 Hz for the first 19 cutting steps, and experienced a zig-zag pattern afterwards caused by the connectivity pattern of nodes in the tetrahedral brick mesh as explained in [17]. This pattern also appeared in the results of the cutting experiments of the beam and brick meshes, as well as the eye mesh as they have a structural pattern in the ellipsoidal shapes.

For brick meshes, AMPS vastly outperformed the unsymmetric augmented matrix method by a factor of 6.37, and the CG method by 11.2. AMPS maintained relatively stable average update rates at 35.6 Hz. The unsymmetric augmented matrix method outperformed CG as constraints were applied to the first dozen nodes, but performance degrades as the number of constrained nodes increased, eventually

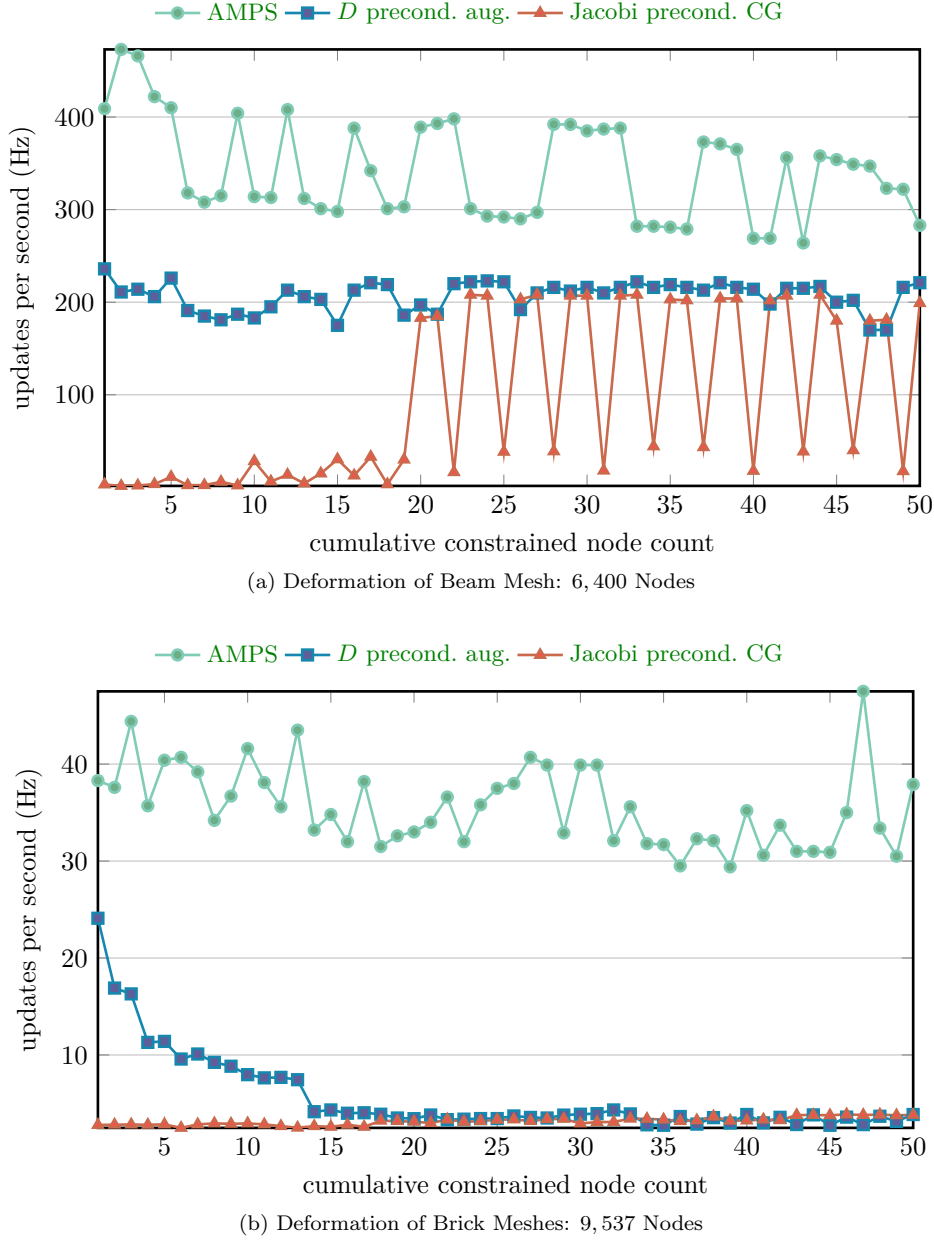
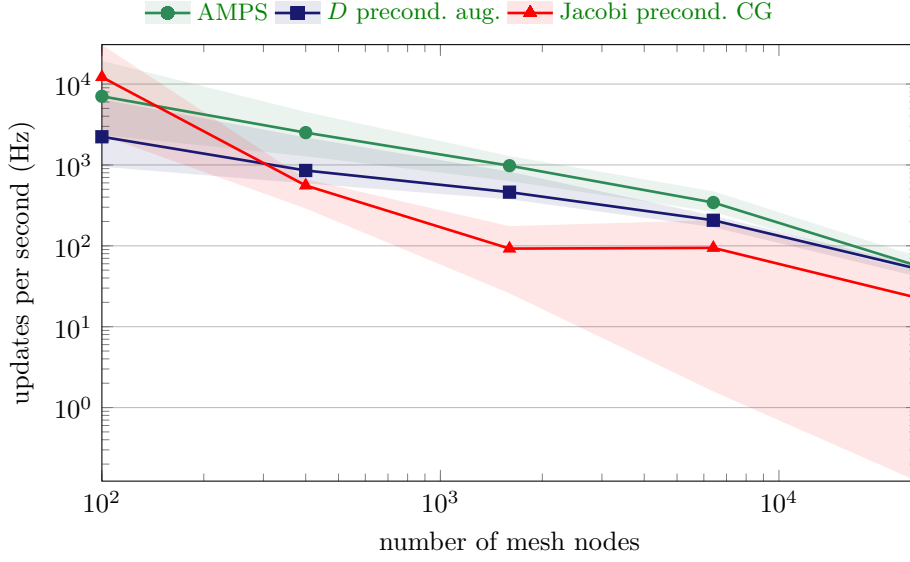


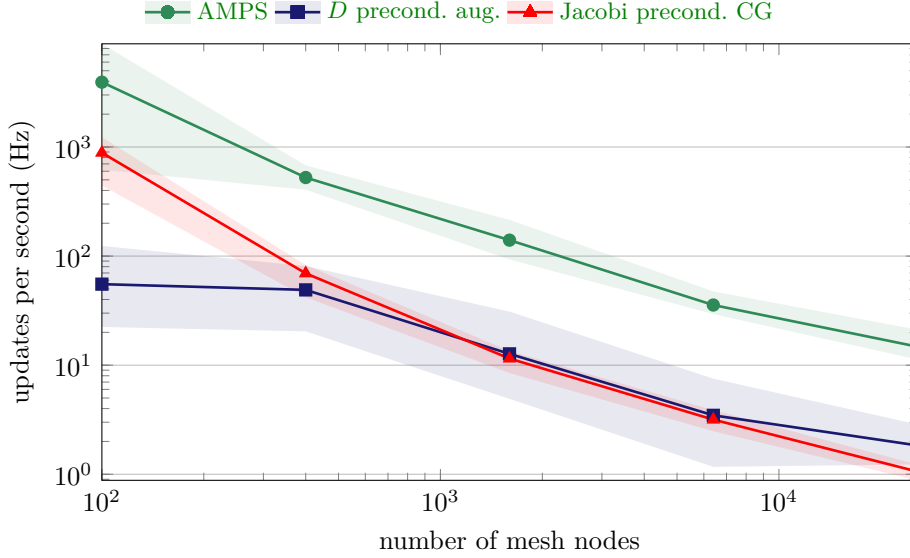
FIG. 4. Deformation update rates are shown for AMPS, the preconditioned augmented and CG methods as constraints are progressively added to an increasing number of nodes in (a) beam and (b) brick meshes.

resulting in similar update rates between the augmented method and CG. Overall, the unsymmetric augmented matrix method achieved an average update rate of 5.59 Hz while the preconditioned CG method only had an average update rate of 3.17 Hz.

Figure 5 is a log-log plot that shows how solution times varied for different sizes of beam and brick meshes. The lines show the trend of the average times for various



(a) Deformation of Beam Meshes



(b) Deformation of Brick Meshes

FIG. 5. Average update rates and ranges are shown for the deformation experiments of the series of (a) beam and (b) brick meshes. AMPS results are shown in green, SPAI preconditioned augmented method results are shown in blue, and Jacobi preconditioned CG results are shown in red.

methods and the shaded areas are the ranges of the solution times. These graphs show that AMPS ran faster than both the augmented and CG methods for the beam meshes except for the very smallest instance that had only 100 nodes. It can also be observed that CG has the largest ranges among all methods especially for the larger beam meshes. This means that the CG solution times increased a lot while

the deformation progressed. For the brick meshes, AMPS also outperformed both the augmented and CG methods with smaller solution time ranges than the other methods.

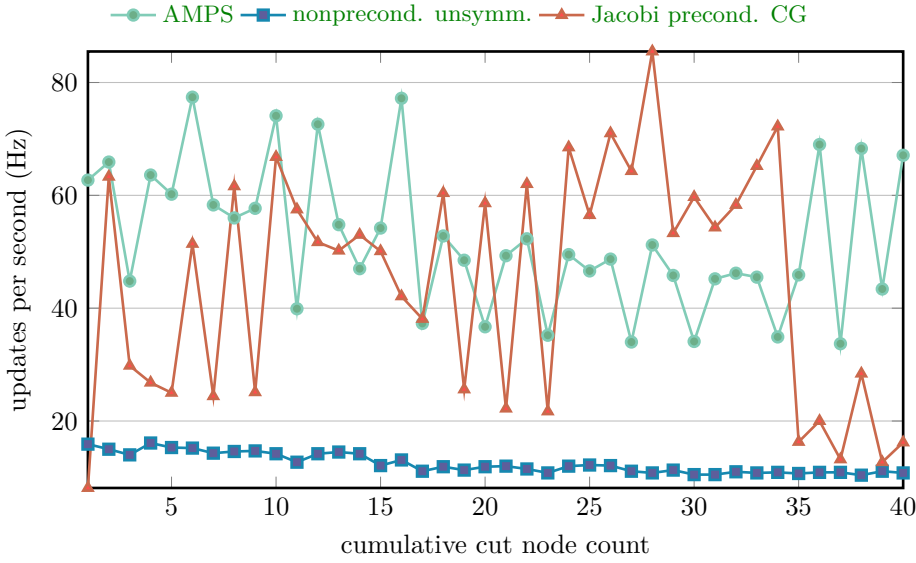
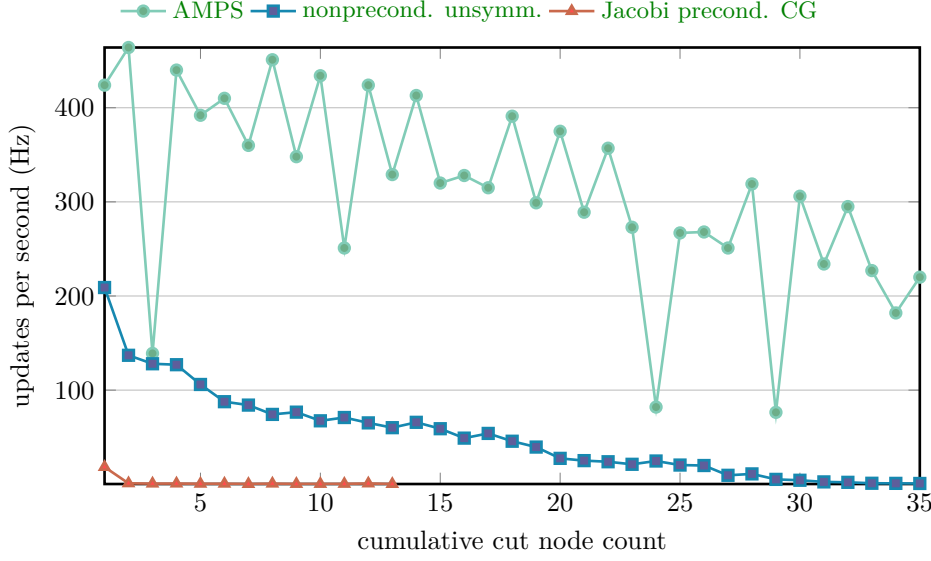
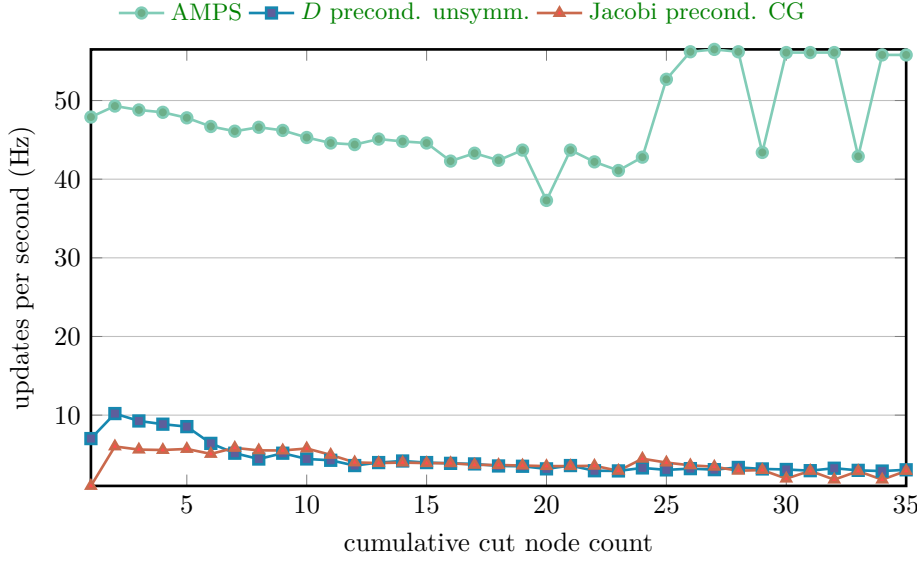
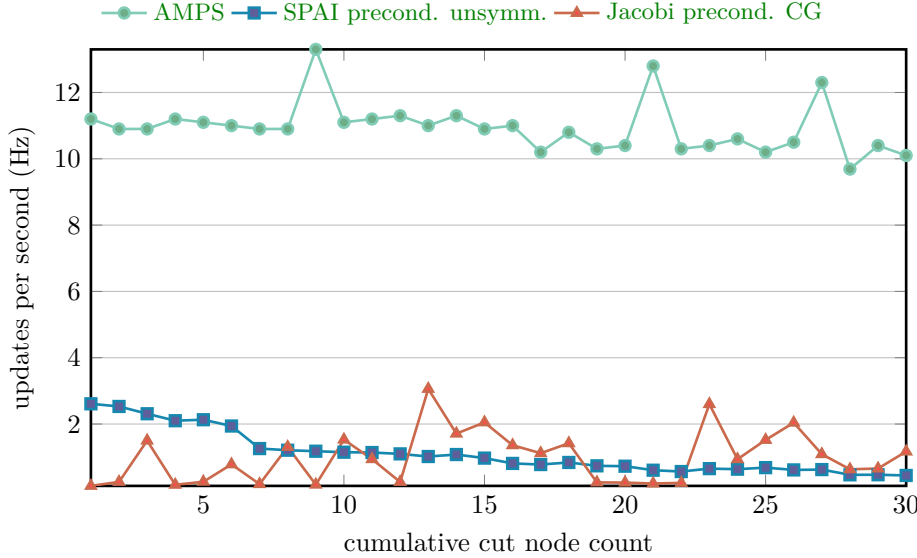


FIG. 6. Update rates are shown for AMPS, the preconditioned augmented and CG methods as a cut is advanced through (a) a beam mesh and (b) a brick mesh.

4.3.2. Deformation of Meshes Undergoing Cutting. In this group of experiments we made an advancing planar cut into the volume of each mesh. As a cut progressed, a copy of each node along the cut path was added to the mesh, and



(a) Astigmatism Surgical Simulation of Eye Mesh: 17,821 Nodes



(b) Cutting of Brain Meshes: 50,737 Nodes

FIG. 7. Timing results are provided for (a) the eye mesh of 17,821 nodes and (b) the brain mesh of 50,737 nodes.

connectivity was modified so that elements on opposite sides of the cut became separated. The newly added node causes the linear system to increase in dimension, and the remeshing associated with the duplicated node and all its neighboring nodes results in a principal submatrix update to the stiffness matrix. In the results, the cut node count corresponds to the number of duplicated nodes resulting from the cut. Opposing force vectors were applied to selected surface nodes to pull the cut faces

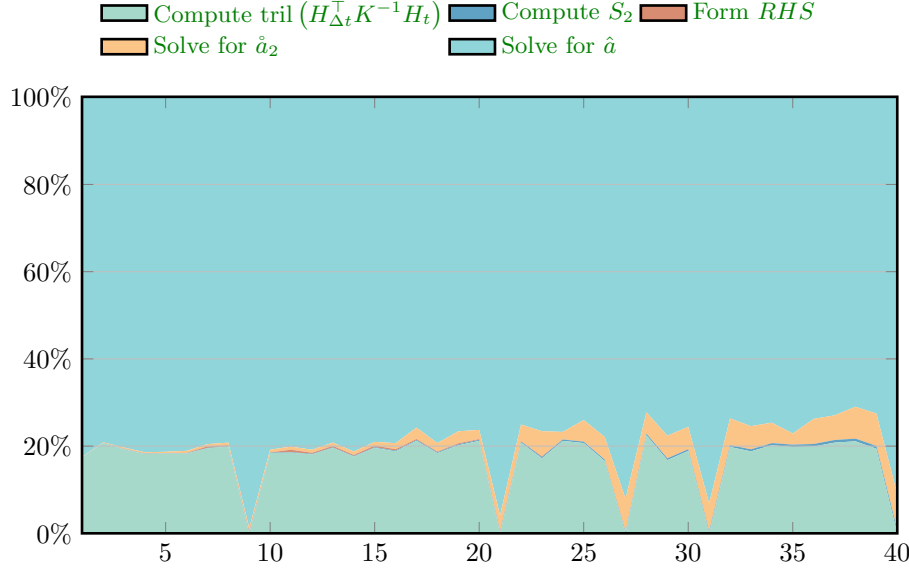


FIG. 8. The breakdown of computation time to steps of AMPS for the brain mesh of 50,737 nodes.

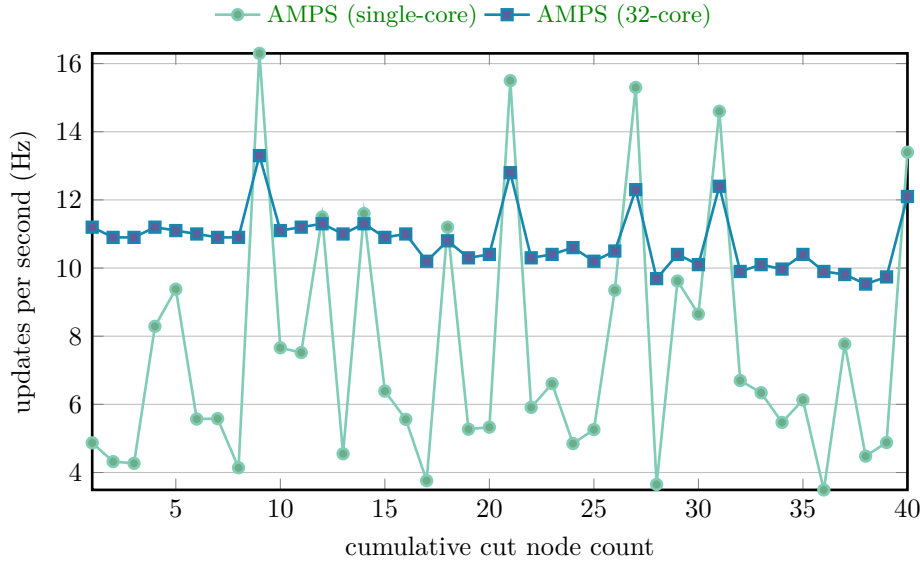


FIG. 9. Single-core and 32-core results are provided for the brain mesh of 50,737 nodes.

apart. Figure 2 shows the the eye mesh at the initial stages of cutting.

While the other methods behaved differently for the cutting and deformation experiments for the beam and brick meshes, AMPS performed similarly between the two experiments as shown in Figure 6a compared to Figure 4. AMPS outperformed the nonpreconditioned unsymmetric augmented matrix method by a factor of 6.06, and Jacobi preconditioned CG method by 216 in the beam cutting experiments, providing updates in the range 167–479 Hz. The unsymmetric augmented method provided

0.83–209 Hz whereas preconditioned CG needed more than 1 second for most of the cutting steps except for the first one, and failed to converge to any solution after the 18th step. D preconditioned and SPAI preconditioned variants ran 15.6 and 12.5 times slower than AMPS respectively. On the other hand, AMPS performed on par with CG for the brick mesh cutting experiment, providing 52.2 Hz and 44.8 Hz update rates; while the unsymmetric augmented matrix method underperformed for this mesh, providing only an average of 12.5 Hz update rate, as shown in Figure 6b. The D preconditioned and SPAI preconditioned variants ran 11.4 and 13.1 times slower than AMPS for the cutting of the brick mesh.

Figure 8 shows the breakdown of the solution times for individual steps of the AMPS algorithm for the brain mesh of 50,737 nodes. The most computational expensive step was the triangular solve for the final solution \hat{a} , accounting for roughly 80% of the time, followed by the computation of the principal submatrix of the inverse, accounting for roughly 20% of the time. The remaining steps are less significant. The valleys in the area plot are due to the fact that at some cuts no additional neighboring vertices were included in $\mathbb{H}_{\Delta t}$ and thus $\text{tril}(H_{\Delta t}^\top K^{-1} H_t)$ is empty and the principal submatrix of the inverse of K need not be updated.

Results from the eye and brain mesh cutting experiments are shown in Figure 7. Here we show that for the astigmatism surgical simulation experiment AMPS vastly outperformed the D preconditioned unsymmetric augmented matrix method by a factor of 10.8 and Jacobi preconditioned CG method by 12.2. For the brain model, AMPS ran 10.2 times faster than the SPAI preconditioned unsymmetric augmented matrix method, 18.5 times faster than the D preconditioned variant, 11.5 times faster than the nonpreconditioned variant, and 11.5 times faster than Jacobi preconditioned CG method. The average update rates of 47.5 Hz and 11.4 Hz achieved by AMPS on both the eye and brain meshes respectively make interactive stimulation feasible.

Figure 9 shows the brain mesh cutting experiments using AMPS on a single core versus 32 cores. Speedups vary for different cuts due to the various numbers of new neighboring nodes of the node being cut. For cuts that do not involve new neighboring nodes, the single-core results are even better than those using 32 cores due to the multi-core overheads. The geometric mean of the speedups is 1.58.

Mesh	$ V $	AMPS	SPAI preconditioned. unsymm. aug.	Jacobi preconditioned. CG
Beam	25,600	7×10^{-11}	$1 \times 10^{-4}(10^{-4})$	failed to converge
Brick	18,081	3×10^{-14}	$5 \times 10^{-5}(10^{-5})$	$5 \times 10^{-5}(10^{-8})$
Eye	17,821	4×10^{-14}	$7 \times 10^{-4}(10^{-5})$	$1 \times 10^{-5}(10^{-7})$
Brain	50,737	9×10^{-14}	$7 \times 10^{-5}(10^{-4})$	$1 \times 10^{-5}(10^{-5})$

TABLE 3

Comparison of relative residual norms ($\|\hat{K}\hat{a} - \hat{f}\|_2 / \|\hat{f}\|_2$). Absolute tolerances for the iterative solvers are listed in parentheses.

Since AMPS uses direct solver in both augmented part and the whole solutions, the solution accuracy of AMPS is only affected by the rounding errors amplified by the matrix condition number. Hence, AMPS not only provided faster update times than both the unsymmetric augmented matrix method and CG methods, but also higher accuracy. Table 3 compares the relative residual norms of the computed solutions of the tested methods. The absolute tolerances listed were set such that the computed

relative residual norms were less than 10^{-3} . If lower tolerances were set, the number of iterations and thus the solution time would increase. It can be observed that the solutions computed by AMPS are much more accurate than the others.

5. Conclusions and Future Work. When meshes are cut, new nodes and elements are inserted during the remeshing, and new boundary conditions are imposed. These changes result in principal submatrix updates to the stiffness system of equations, and we have demonstrated that the solutions of the modified systems can be computed in real-time with high accuracy even for large meshes. Our new AMPS algorithm has outperformed an earlier unsymmetric augmented method and CG in almost every deformation and cutting experiment. We have also observed that unlike the unsymmetric augmented method, the update rates of AMPS do not deteriorate while the number of constrained nodes increases, or the cutting is being advanced in the meshes. These properties of AMPS are crucial for making real-time surgical simulation feasible as it requires accurate, fast and stable updates to the meshes. Refactorization would not be needed when AMPS is applied.

As we observed from the experimental results, the computation time for the augmentation is no longer the dominating factor of the total solution time for large meshes. More time was spent on the triangular solves in the solution. Hence, in the future one could incorporate the parallelization of the triangular solves into the AMPS algorithm. For more complicated and larger meshes, GPU and distributed parallelism could also be explored.

The surgical simulations community has found the linear elastic model to be useful for biomechanical modeling when deformations are small and limited forces are applied, although linear elasticity does not adequately model organs and tissue types under heavier loading scenarios. Nonlinear models are not considered in this article, but could be investigated in the future for a broader range of surgical simulation problems, since there is evidence that viscoelastic and hyperelastic material models are often appropriate for modeling soft tissues [6] [9] [11].

REFERENCES

- [1] J. CROUCH AND A. CHERRY, *Parametric eye models*, in Medicine meets virtual reality, J. Westwood, R. Haluck, H. Hoffman, G. Mogel, R. Phillips, R. Robb, and K. Vosburgh, eds., vol. 15, Jan. 2007, pp. 91–93.
- [2] J. CROUCH, S. PIZER, E. CHANEY, Y.-C. HU, G. MAGERAS, AND M. ZAIDER, *Automated finite element analysis for deformable registration of prostate images*, IEEE Trans. on Med. Imag., 26 (2007), pp. 1379–1390, <https://doi.org/10.1109/TMI.2007.898810>.
- [3] T. A. DAVIS AND W. W. HAGER, *Row modifications of a sparse Cholesky factorization*, SIAM Journal on Matrix Analysis and Applications, 26 (2005), pp. 621–639, <https://doi.org/10.1137/S089547980343641X>.
- [4] F. DOBRIAN AND A. POTHE, *Oblivio: Design and performance*, in Applied Parallel Computing. State of the Art in Scientific Computing, J. Dongarra, K. Madsen, and J. Wasniewski, eds., vol. 3732 of Lecture Notes in Computer Science, Springer Berlin Heidelberg, 2006, pp. 758–767, https://doi.org/10.1007/11558958_92.
- [5] C. FOREST, H. DELINGETTE, AND N. AYACHE, *Cutting simulation of manifold volumetric meshes*, in Proc. of Int. Conf. Medical Image Computing and Computer-Assisted Intervention, Part II, London, UK, 2002, Springer-Verlag, pp. 235–244.
- [6] Y. FUNG, *Biomechanics: Mechanical Properties of Living Tissues*, Springer-Verlag, 1993.
- [7] O. GOKSEL AND S. SALCUDEAN, *Image-based variational meshing*, IEEE Trans. on Medical Imaging, 30 (2011), pp. 11–21, <https://doi.org/10.1109/TMI.2010.2055884>.
- [8] INTEL CORPORATION, *Math Kernel Library Developer Reference*, 2015, <https://software.intel.com/en-us/articles/mkl-reference-manual>.
- [9] R. LAPEER, P. GASSON, AND V. KARRI, *Simulating plastic surgery: From human skin tensile tests, through hyperelastic finite element models to real-time haptics*, Progress in Biophysics

- & Molecular Biology, 103 (2010), pp. 208–216, <https://doi.org/10.1016/j.pbiomolbio.2010.09.013>.
- [10] C. LEDERMAN, A. JOSHI, I. DINOV, J. VAN HORN, L. VESE, AND A. TOGA, *Tetrahedral mesh generation for medical images with multiple regions using active surfaces*, in IEEE Int. Symp. Biomedical Imaging: From Nano to Macro, Apr. 2010, pp. 436–439, <https://doi.org/10.1109/ISBI.2010.5490317>.
 - [11] S. MARCHESSEAU, T. HEIMANN, S. CHATELIN, R. WILLINGER, AND H. DELINGETTE, *Fast porous visco-hyperelastic soft tissue model for surgery simulation: Application to liver surgery*, Progress in Biophysics & Molecular Biology, 103 (2010), pp. 185–196, <https://doi.org/10.1016/j.pbiomolbio.2010.09.005>.
 - [12] A. MOHAMED AND C. DAVATZIKOS, *Finite element mesh generation and remeshing from segmented medical images*, in IEEE Int. Symp. Biomedical Imaging: Nano to Macro, vol. 1, Apr. 2004, pp. 420–423, <https://doi.org/10.1109/ISBI.2004.1398564>.
 - [13] A. MOR AND T. KANADE, *Modifying soft tissue models: Progressive cutting with minimal new element creation*, in Medical Image Computing and Computer-Assisted Intervention, S. Delp, A. DiGoia, and B. Jaramaz, eds., vol. 1935 of Lecture Notes in Computer Science, Springer Berlin / Heidelberg, 2000, pp. CH412–CH412.
 - [14] J. SPILLMANN AND M. HARDERS, *Robust interactive collision handling between tools and thin volumetric objects*, IEEE Trans. on Visualization and Computer Graphics, 18 (2012), pp. 1241–1254, <https://doi.org/10.1109/TVCG.2011.151>.
 - [15] D. STEINEMANN, M. HARDERS, M. GROSS, AND G. SZEKELY, *Hybrid cutting of deformable solids*, in Prof. of IEEE Virtual Reality, Mar. 2006, pp. 35–42, <https://doi.org/10.1109/VR.2006.74>.
 - [16] M. TESCHNER, S. KIMMERLE, B. HEIDELBERGER, G. ZACHMANN, L. RAGHUPATHI, A. FUHRMANN, M.-P. CANI, F. FAURE, N. MAGNENAT-THALMANN, W. STRASSER, AND P. VOLINO, *Collision detection for deformable objects*, 2005, <https://doi.org/10.1111/j.1467-8659.2005.00829.x>.
 - [17] Y.-H. YEUNG, J. CROUCH, AND A. POTHEN, *Interactively cutting and constraining vertices in meshes using augmented matrices*, ACM Trans. Graph., 35 (2016), pp. 18:1–18:17, <https://doi.org/10.1145/2856317>.
 - [18] Y.-H. YEUNG, A. POTHEN, M. HALAPPANAVAR, AND Z. HUANG, *AMPS: An augmented matrix formulation for principal submatrix updates with application to power grids*, SIAM J. Scientific Computing, (2017). to appear.
 - [19] X. ZHANG AND Y. KIM, *Simple culling methods for continuous collision detection of deforming triangles*, IEEE Trans. on Visualization and Computer Graphics, 18 (2012), pp. 1146–1155, <https://doi.org/10.1109/TVCG.2011.120>.